(Received 17 April 2025, Accepted 18 June 2025, Scheduled 1 July 2025)

Research on Coherent Integration for Maneuvering Target Detection Based on KT-ITDCI

Aihua Li[1], Wei Liu[1], Yuhang Wang[2], Wenwen Xu[2], Jianyin Cao[2], and Hao Wang[2,*]

[1] *Beijing Institute of Remote Sensing Equipment, Beijing 100854, China*
[2] *School of Electronic & Optical Engineering, Nanjing University of Science and Technology, Nanjing 210094, China*

ABSTRACT: In order to enhance the detection capability of maneuvering targets, long-time coherent integration (LTCI) is widely employed. The core idea of LTCI is to coherently integrate signal energy over an extended observation period, thereby enhancing the signal-to-noise ratio (SNR). However, for maneuvering targets, defocusing may occur due to range migration (RM) and Doppler frequency migration (DFM). In this study, a novel method based on the keystone transform and improved 3-D coherent integration (KT-ITDCI) for maneuvering target detection is proposed. KT-ITDCI not only eliminates the RM induced by unambiguous velocity through KT, but also compensates for residual RM and DFM in the KT-processed echoes via ITDCI, ultimately achieving coherent integration. Simulation results show that, compared with the TDCI method, KT-ITDCI significantly reduces computational complexity while maintaining comparable anti-noise performance. Furthermore, the effectiveness of the proposed method is validated through processing and analyzing real measured radar data.

1. INTRODUCTION

In order to enhance the detection capability for maneuvering targets, long-time coherent integration (LTCI) is widely employed [1–5]. LTCI improves the signal-to-noise ratio (SNR) by coherently integrating signal energy over an extended observation period. However, due to target maneuverability during the observation period, range migration (RM) and Doppler frequency migration (DFM) are likely to occur, which significantly degrade integration performance [6–10]. Therefore, correcting RM and DFM is essential for improving integration gains.

Extensive studies have been conducted on LTCI for maneuvering target signals. For uniformly moving targets, RM can be typically corrected using the keystone transform (KT) [11], Radon Fourier transform (RFT) [12], adjacent cross correlation function (ACCF) [13], and sequence reversing transform (SRT) [14]. For targets undergoing uniform acceleration, one approach is based on motion parameter search. Representative methods include the generalized RFT (GRFT) [15], Radon-fractional Fourier transform (RFRFT) [16], and Radon-Lv's distribution (RLVD) [17]. Such search-based methods exhibit excellent anti-noise performance but suffer from high computational complexity. An alternative approach first corrects RM and then represents the target echo as a linear frequency-modulated (LFM) signal in the slow-time domain, where the acceleration is estimated by extracting the chirp rate of the LFM signal. Several notable methods include the improved axis rotation-fractional Fourier transform (IAR-FRFT) [18], KT-LVD [19], and symmetric autocorrelation function-scaled Fourier transform (SAF-SFT) [20]. These approaches reduce computational complexity compared to search-based methods but degrade anti-noise performance.

Another approach is to estimate motion parameters of targets simultaneously, including the 3-D scaled transform (TDST) [21] and 3-D coherent integration (TDCI) [22]. These methods offer a balance between anti-noise performance and computational complexity, making them more practical for real-time applications. Specifically, the TDCI method constructs a 3-D autocorrelation function (AF) based on the received echo signals. Through a series of operations, such as the fast Fourier transform (FFT), nonuniform FFT (NUFFT), and scaled Fourier transform (SFT), signal energy is gradually integrated. However, TDCI requires multiple SFT operations on the 3-D AF, which results in high computational complexity. Additionally, due to high target speed and low pulse repetition frequency (PRF), undersampling occurs, causing velocity ambiguity [19]. The incorporation of AF exacerbates undersampling, further increasing the computational burden of the compensation process in TDCI.

To address these challenges, this paper proposes a novel coherent integration method based on KT and improved TDCI (KT-ITDCI). KT-ITDCI not only eliminates the RM induced by unambiguous velocity through KT, but also compensates for residual RM and DFM in the KT-processed echoes via ITDCI, ultimately achieving coherent integration. Extensive simulations are conducted to validate the effectiveness of the proposed method. Finally, real-world measurement data are analyzed to further demonstrate its practical applicability and effectiveness.

Compared with TDCI, the proposed method introduces several improvements that significantly reduce computa-

* Corresponding author: Hao Wang (haowang@njust.edu.cn).

tional complexity, while maintaining detection performance comparable to that of TDCI. These improvements include:

- The SFT of the 3-D data is replaced by applying an SFT and an inverse FFT (IFFT) to the 2-D data, followed by an FFT applied to the 3-D data. Notably, the combination of the SFT and IFFT is equivalent to the KT.
- The introduction of the KT first corrects the RM caused by unambiguous velocity under undersampling conditions, thereby preventing further undersampling issues during AF construction.
- A scaling factor is introduced in the NUFFT operation, allowing flexible adjustment of the acceleration estimation range and accuracy under different radar system parameters.

The rest of this paper is organized as follows. In Section 2, a signal model is established. The proposed method is described in detail in Section 3. Then, experimental results are presented in Section 4. Finally, conclusions are given in Section 5.

2. SIGNAL MODEL

Assume that the radar transmits a LFM signal as follows [22]

$$s_{\mathrm{t}}(t)=\mathrm{rect}\left(\frac{t}{T_p}\right)\exp\left(\mathrm{j}\pi\mu t^2\right)\exp\left(\mathrm{j}2\pi f_c t\right), \tag{1}$$

where $\mathrm{rect}\left(x\right)=\begin{cases}1, & |x|\le 1/2\\ 0, & |x|>1/2\end{cases}$, t is the fast time, T_P the pulsewidth, μ the frequency modulated rate, and f_c the carrier frequency.

The received signal can be expressed as

$$\begin{aligned}s_{\mathrm{r}}\left(t,t_m\right) &= A_{in}\mathrm{rect}\left[\frac{t-2R(t_m)/c}{T_P}\right]\exp\left[-j\frac{4\pi f_c}{c}R(t_m)\right]\\ &\times\exp\left\{j\pi\mu\left[t-\frac{2R(t_m)}{c}\right]^2\right\},\end{aligned} \tag{2}$$

where A_{in} is the signal amplitude, $R(t_m)$ the slant range between radar and the target, $t_m=mT_r\ (m=0,\ldots,M-1)$ the slow time, T_r the pulse repetition interval, and M the number of radar pulses.

After down conversion and pulse compression (PC) in (2), the processed result is given by

$$s_{\mathrm{p}}\left(t,t_m\right)=A\mathrm{sinc}\left\{B\left[t-\frac{2R\left(t_m\right)}{c}\right]\right\}\exp\left[-\mathrm{j}\frac{4\pi f_c}{c}R(t_m)\right], \tag{3}$$

where A is the amplitude of the compressed signal, and B is the signal bandwidth.

For targets undergoing uniform acceleration, $R(t_m)$ satisfies [19]

$$R(t_m)=R_0+\left(v_0+nv_m\right)t_m+\frac{1}{2}at_m^2, \tag{4}$$

where R_0 is the initial slant range, a the radial acceleration, n the fold factor, $v_m=\lambda f_p/2$ the blind velocity, and $v_0=\mathrm{mod}(v,v_m)$ the unambiguous velocity which satisfies $|v_0|<v_m/2$.

Substituting (4) into (3) yields

$$\begin{aligned}s_{\mathrm{p}}(t,t_m)=&A_0\mathrm{sinc}\left\{B\left[t-\frac{2\left(R_0+v_0t_m+nv_mt_m+\frac{1}{2}at_m^2\right)}{c}\right]\right\}\\ &\times\exp\left[-\mathrm{j}\frac{4\pi}{\lambda}\left(R_0+v_0t_m+nv_mt_m+\frac{1}{2}at_m^2\right)\right],\end{aligned} \tag{5}$$

where $\lambda=c/f_c$ is the signal wavelength, and $\exp\left(-\mathrm{j}4\pi nv_mt_m/\lambda\right)=1$ [19].

The Doppler frequency is given by

$$f_{\mathrm{d}}=\frac{1}{2\pi}\cdot\frac{\mathrm{d}\left[-\frac{4\pi}{\lambda}\left(R_0+v_0t_m+\frac{1}{2}at_m^2\right)\right]}{\mathrm{d}t_m}=-\frac{2\left(v_0+at_m\right)}{\lambda}. \tag{6}$$

Equations (5) and (6) reveal that, after PC, the envelope of the echo signal varies with slow time. RM occurs when the offset exceeds the range resolution, while acceleration-induced Doppler frequency variation causes DFM when it surpasses the Doppler frequency resolution.

3. PRINCIPLE OF KT-ITDCI

In this section, KT-ITDCI is introduced to correct RM and DFM for coherent integration and motion parameter estimation.

3.1. RM Correction via KT

Applying FFT to (5) with respect to t yields

$$\begin{aligned}s_{\mathrm{p}}(f,t_m)=&A_0\mathrm{rect}\left(\frac{f}{B}\right)\exp\left(-\mathrm{j}\frac{4\pi f}{c}nv_mt_m\right)\\ &\times\exp\left[-\mathrm{j}\frac{4\pi(f+f_c)}{c}\left(R_0+v_0t_m+\frac{1}{2}at_m^2\right)\right]\end{aligned} \tag{7}$$

where A_0 is the signal amplitude, f the range frequency, and $\exp(-\mathrm{j}4\pi fnv_mt_m/c)=\exp(-\mathrm{j}2\pi nt_mf_pf/f_c)$. In fact, RM results from the coupling between f and t_m, and DFM results from the coupling between f_c and t_m squared.

KT is a scaled operation performed on (7) to eliminate the RM caused by unambiguous velocity, whose scaling formula is expressed as

$$t_m=\frac{f_c}{f+f_c}t'_m, \tag{8}$$

where t'_m is the scaled slow time. KT can be efficiently implemented using a combination of SFT and IFFT.

Substituting (8) into (7) yields

$$\begin{aligned}s_{\mathrm{p}}(f,t'_m)=&A_0\mathrm{rect}\left(\frac{f}{B}\right)\exp\left[-\mathrm{j}\frac{4\pi\left(f+f_c\right)}{c}R_0\right]\\ &\times\exp\left(-\mathrm{j}\frac{4\pi}{\lambda}v_0t'_m\right)\exp\left[-\mathrm{j}\frac{2\pi}{\lambda}\left(\frac{f_c}{f+f_c}\right)at_m'^2\right]\end{aligned}$$

$$\times \exp\left[\mathrm{j}\frac{4\pi}{\lambda}\left(\frac{f_c}{f+f_c}\right)nv_m t'_m\right]. \quad (9)$$

In (9), the coupling among f, v_0, and t_m is removed, which effectively corrects RM caused by unambiguous velocity. However, the RM caused by undersampling and acceleration, and DFM caused by acceleration still persist and require further compensation.

3.2. Integration via ITDCI

A 3-D AF is introduced and defined as

$$R\left(f,t'_m,\tau\right)=s_{\mathrm{p}}\left[f,t'_m+(\tau+\tau_c)\right]s_{\mathrm{p}}\left[f,t'_m-(\tau+\tau_c)\right], \quad (10)$$

where τ is a lag time variable, and τ_c is a constant lag time.

Substituting (9) into (10), the result is given by

$$\begin{aligned}R(f,t'_m,\tau)=&A_1\mathrm{rect}\left(\frac{f}{B}\right)\exp\left(-\mathrm{j}\frac{8\pi f}{c}R_0\right)\exp\left(-\mathrm{j}\frac{8\pi}{\lambda}v_0t'_m\right)\\&\times\exp\left\{-\mathrm{j}\frac{4\pi}{\lambda}\left(\frac{f_c}{f+f_c}\right)a\left[t'^2_m+(\tau+\tau_c)^2\right]\right\}\\&\times\exp\left[\mathrm{j}\frac{4\pi}{\lambda}\left(\frac{f_c}{f+f_c}\right)nv_mt'_m\right]. \quad (11)\end{aligned}$$

where $A_1=A_0^2\exp(-\mathrm{j}8\pi R_0/\lambda)$ is the signal amplitude.

The 1st coherent integration is achieved via the NUFFT to (11) with respect to $(\tau+\tau_c)$, i.e.,

$$\begin{aligned}&C_1\left(f,t'_m,f_\tau\right)\\&=\int R\left(f,t'_m,\tau\right)\exp\left[-\mathrm{j}2\pi f_\tau\left(\frac{f_c}{f+f_c}\right)\frac{(\tau+\tau_c)^2}{h}\right]\mathrm{d}\tau_m\\&=A_2\mathrm{rect}\left(\frac{f}{B}\right)\exp\left(-\mathrm{j}\frac{8\pi f}{c}R_0\right)\exp\left(-\mathrm{j}\frac{8\pi}{\lambda}v_0t'_m\right)\\&\quad\times\exp\left[-\mathrm{j}\frac{4\pi}{\lambda}\left(\frac{f_c}{f+f_c}\right)at'^2_m\right]\delta\left(f_\tau+\frac{2a}{h\lambda}\right)\\&\quad\times\exp\left[\mathrm{j}\frac{4\pi}{\lambda}\left(\frac{f_c}{f+f_c}\right)nv_mt'_m\right], \quad (12)\end{aligned}$$

where A_2 is the signal amplitude, f_τ the scaled frequency variable with respect to τ, and h a scaling factor.

In (12), the energy is concentrated into planes $f_\tau=-2ah/\lambda$. At this point, the estimation accuracy is $\lambda f_\tau/2hM$, with an estimation range of $[-\lambda f_\tau/4h,\lambda f_\tau/4h]$. The estimation accuracy and range of acceleration can be adjusted by modifying the scaling factor.

Afterwards, the coupling between λ and t'^2_m can be removed by the dechirp processing (DP), presented as

$$\begin{aligned}&C'_1\left(f,t'_m,f_\tau\right)\\&=C_1\left(f,t'_m,f_\tau\right)\exp\left[-\mathrm{j}2\pi\left(\frac{f_c}{f+f_c}\right)hf_\tau t'^2_m\right]\\&=A_2\mathrm{rect}\left(\frac{f}{B}\right)\exp\left(-\mathrm{j}\frac{8\pi f}{c}R_0\right)\exp\left(-\mathrm{j}\frac{8\pi}{\lambda}v_0t'_m\right)\\&\quad\times\delta\left(f_\tau+\frac{2ah}{\lambda}\right)\exp\left[\mathrm{j}\frac{4\pi}{\lambda}\left(\frac{f_c}{f+f_c}\right)nv_mt'_m\right]. \quad (13)\end{aligned}$$

Next, all possible fold factors n_t are iterated through to construct the phase compensation function for undersampling compensation (UC) in (13), which can be expressed as

$$H_1\left(f,t'_m;n_t\right)=\exp\left[-\mathrm{j}\frac{4\pi}{\lambda}\left(\frac{f_c}{f+f_c}\right)n_tv_mt'_m\right], \quad (14)$$

When $n_t=n$, multiplying (13) by (14) yields

$$\begin{aligned}C_1^{n_t}\left(f,t'_m,f_\tau\right)=&A_2\mathrm{rect}\left(\frac{f}{B}\right)\exp\left(-\mathrm{j}\frac{8\pi f}{c}R_0\right)\\&\times\exp\left(-\mathrm{j}\frac{8\pi}{\lambda}v_0t'_m\right)\delta\left(f_\tau+\frac{2ah}{\lambda}\right). \quad (15)\end{aligned}$$

Thereafter, the 2nd coherent integration is achieved via the FFT to (15) with respect to t'_m, i.e.,

$$\begin{aligned}C_2^{n_t}\left(f,f_{t'_m},f_\tau\right)=&A_3\mathrm{rect}\left(\frac{f}{B}\right)\exp\left(-\mathrm{j}\frac{8\pi f}{c}R_0\right)\\&\times\delta\left(f_{t'_m}+\frac{4v_0}{\lambda}\right)\delta\left(f_\tau+\frac{2ah}{\lambda}\right). \quad (16)\end{aligned}$$

where A_3 is the signal amplitude.

The final coherent integration is achieved via the IFFT to (16) with respect to f, resulting in the ITDCI domain, i.e.,

$$\begin{aligned}C_3^{n_t}(t,f_{t'_m},f_\tau)=&A_4\mathrm{sinc}\left[B\left(t-\frac{4R_0}{c}\right)\right]\delta\left(f_{t'_m}+\frac{4v_0}{\lambda}\right)\\&\times\delta\left(f_\tau+\frac{2ah}{\lambda}\right) \quad (17)\end{aligned}$$

where A_4 is the signal amplitude.

Figure 1 shows the diagram of ITDCI method, where the dark shading indicates the energy of the target signal.

From (17), it is observed that the result contains a unique peak at $(4R_0/c,-4v_0/\lambda,-2ah/\lambda)$, allowing the motion parameters to be estimated via peak detection. However, the unambiguous velocity information obtained here may result from further undersampling after AF. To obtain accurate unambiguous velocity information, a phase compensation function is constructed, i.e.,

$$H(f,t'_m;a,n)=\exp\left[-\mathrm{j}\frac{4\pi}{\lambda}\left(\frac{f_c}{f+f_c}\right)\left(nv_mt'_m-\frac{1}{2}at'^2_m\right)\right]. \quad (18)$$

Multiplying (18) with (9) yields

$$\begin{aligned}s'_{\mathrm{p}}\left(f,t'_m\right)=&A_0\mathrm{rect}\left(\frac{f}{B}\right)\exp\left[-\mathrm{j}\frac{4\pi\left(f+f_c\right)}{c}R_0\right]\\&\times\exp\left(-\mathrm{j}\frac{4\pi}{\lambda}v_0t'_m\right). \quad (19)\end{aligned}$$

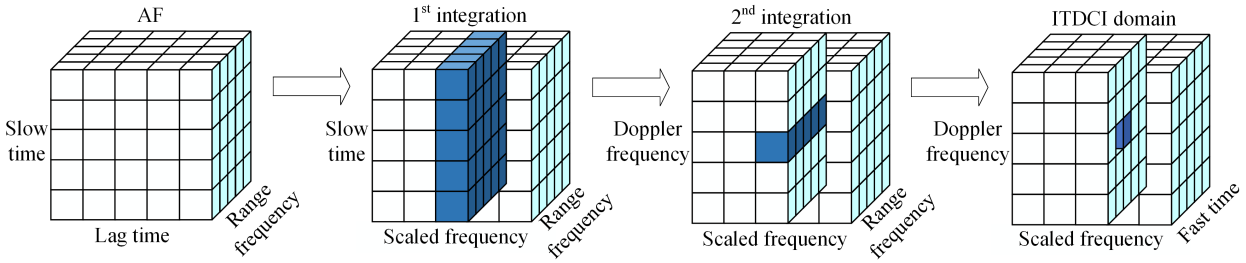

FIGURE 1. Diagram of the ITDCI method.

Applying IFFT to (19) with respect to f yields

$$s'_{\mathrm{p}}(t,t'_m)=A\mathrm{sinc}\left[B\left(t-\frac{2R_0}{c}\right)\right]\exp\left[-\mathrm{j}\frac{4\pi}{\lambda}(R_0+v_0t'_m)\right]. \tag{20}$$

Finally, the coherent integration can be achieved by applying an FFT to (20) with respect to t'_m, and the result is given by

$$s'_{\mathrm{p}}\left(t,f_{t'_m}\right)=A_4\mathrm{sinc}\left[B\left(t-\frac{2R_0}{c}\right)\right]\delta\left(f_{t'_m}+\frac{2v_0}{\lambda}\right), \tag{21}$$

where A_4 is the signal amplitude.

From (21), it is observed that the result contains a unique peak at $(2R_0/c,-2v_0/\lambda)$. A constant false alarm rate (CFAR) detector is then applied to detect the target and estimate the unambiguous velocity.

A flowchart of the proposed KT-ITDCI method is illustrated in Fig. 2.

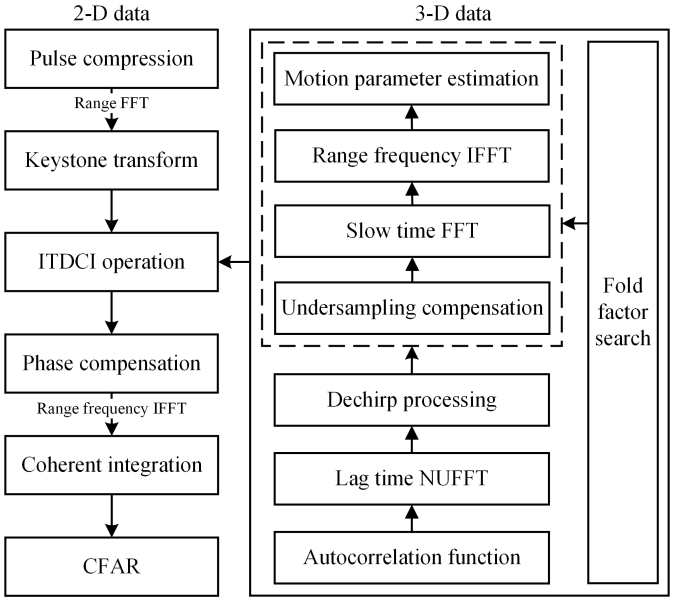

FIGURE 2. Flowchart of the proposed KT-ITDCI method.

3.3. Cross Terms

Since KT is a linear transformation, no cross terms are generated [7]. The cross terms in the proposed ITDCI method are analyzed below.

Considering the scenario with multiple targets, (9) can be rewritten as

$$\begin{aligned}s_{\mathrm{p}}(f,t'_m)=&\sum_{i=1}^{k}A_i\mathrm{rect}\left(\frac{f}{B}\right)\exp\left[-\mathrm{j}\frac{4\pi\left(f+f_c\right)}{c}R_{0i}\right]\\&\times\exp\left(-\mathrm{j}\frac{4\pi}{\lambda}v_{0i}t'_m\right)\exp\left[-\mathrm{j}\frac{2\pi}{\lambda}\left(\frac{f_c}{f+f_c}\right)a_it'^2_m\right]\\&\times\exp\left[-\mathrm{j}\frac{4\pi}{\lambda}\left(\frac{f}{f+f_c}\right)n_iv_mt'_m\right],\end{aligned} \tag{22}$$

where A_i, R_{0i}, v_{0i}, a_i, n_i denote the signal amplitude, initial slant range, radial unambiguous velocity, radial acceleration, and fold factor of the i-th target, respectively. A total of k targets are considered.

Substituting (22) into (10), the constructed AF can be expressed as

$$\begin{aligned}&R\left(f,t'_m,\tau\right)\\&=A_{pq}\mathrm{rect}\left(\frac{f}{B}\right)\exp\left(-\mathrm{j}\frac{4\pi f}{c}\nabla R\right)\exp\left(-\mathrm{j}\frac{8\pi}{\lambda}\nabla v_0t'_m\right)\\&\times\exp\left\{-\mathrm{j}\frac{4\pi}{\lambda}\left(\frac{f_c}{f+f_c}\right)\nabla a\left[t'^2_m+(\tau+\tau_c)^2\right]\right\}\\&\times\exp\left[\mathrm{j}\frac{4\pi}{\lambda}\left(\frac{f_c}{f+f_c}\right)\nabla nv_mt'_m\right]+R_c\left(f,t'_m,\tau\right),\end{aligned} \tag{23}$$

where

$$\begin{aligned}R_c\left(f,t'_m,\tau\right)=&\exp\left[-\mathrm{j}\frac{4\pi}{\lambda}\Delta v_0\left(\tau+\tau_c\right)\right]\\&\times\exp\left[-j\frac{4\pi}{\lambda}\left(\frac{f_c}{f+f_c}\right)\Delta at'_m\left(\tau+\tau_c\right)\right]\\&\times\exp\left[\mathrm{j}\frac{4\pi}{\lambda}\left(\frac{f_c}{f+f_c}\right)\Delta nv_m(\tau+\tau_c)\right],\end{aligned} \tag{24}$$

A_{pq} denotes the signal amplitude, $\nabla R_0=R_{0p}+R_{0q}$, $\Delta n=n_p-n_q$, $\nabla n=n_p+n_q$, $\Delta a=a_p-a_q$, $\nabla a=a_p+a_q$, $\Delta v_0=v_{0p}-v_{0q}$, and $\nabla v_0=v_{0p}+v_{0q}$.

It can be observed that all phase terms in (24) are linearly related to $(\tau+\tau_c)$. After applying the NUFFT to (24) with respect to $(\tau+\tau_c)$, an additional quadratic phase term is introduced into the signal, causing energy dispersion and making the entire cross terms spread in ITDCI domain, preventing effective coherent integration. Thus, the KT-ITDCI method has an effective inhibitory effect on the cross terms generated between different targets.

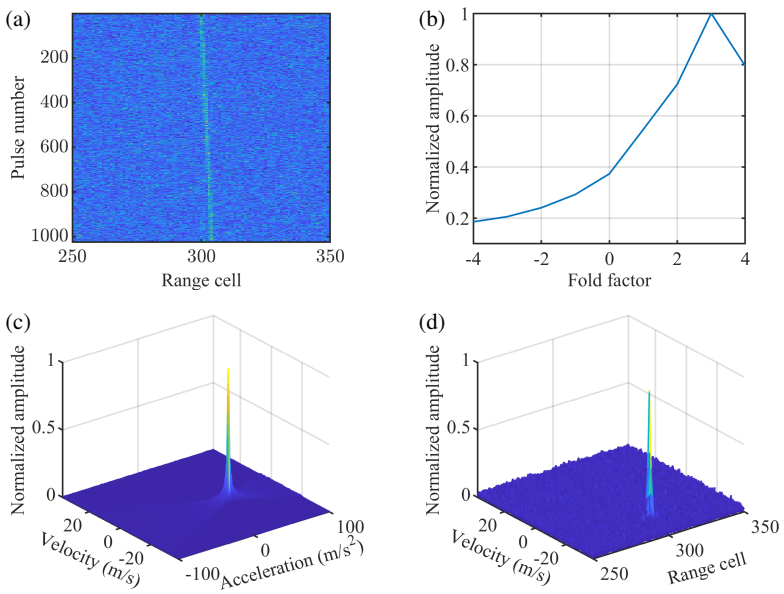

FIGURE 3. Simulation results of the proposed method. (a) Result after PC. (b) Fold factor search result. (c) Acceleration estimation result. (d) Coherent integration result.

4. EXPERIMENTAL RESULTS

In this section, the effectiveness of the proposed method is evaluated through both simulation and real data processing.

4.1. Coherent Integration for a Weak Target

The radar parameters and target motion parameters are listed in Table 1 and Table 2, respectively. After PC, the simulated signal attained an SNR of 3 dB, with significant RM observed in Fig. 3(a). The simulation results of the proposed method are presented in Figs. 3(b)–(d), demonstrating that the KT-ITDCI method effectively achieves coherent integration.

TABLE 1. Simulation parameters of radar.

Parameters	Value
Carrier frequency	10 GHz
PRF	5 kHz
Pulse width	10 μs
Bandwidth	10 MHz
Sampling frequency	15 MHz
Pulse number	1024

TABLE 2. Simulation parameters of a single target.

Parameters	Value
Initial range cell	300
Velocity	200 m/s
Acceleration	30 m/s^2

4.2. Coherent Integration for Multiple Targets

The following simulation aims to verify the multi-objective processing capability of the method. The radar system parameters are identical to those in Table 1, and the multiple motion parameters are summarized in Table 3.

TABLE 3. Simulation parameters of multiple targets.

Parameters	Target A	Target B	Target C
Initial range cell	300	300	300
Velocity	200 m/s	200 m/s	220 m/s
Acceleration	30 m/s^2	10 m/s^2	30 m/s^2

Figure 4(a) shows the result after PC. Due to the similarity of the motion parameters of the three targets, their motion trajectories are closely intertwined. The outcome of the fold factor search is shown in Fig. 4(b), followed by the acceleration estimation result in Fig. 4(c). The three distinct energy peaks in Fig. 4(c) indicate that the ITDCI method successfully separates and accurately estimates multiple targets' motion parameters. This result also verifies the proposed method's capability to effectively suppress cross terms. Figs. 4(d)–(f) present the coherent integration results. Due to the similar velocities and identical accelerations of Targets A and C, their results in Fig. 4(d) and Fig. 4(f) appear notably similar.

4.3. Computational Complexity

In this section, GRFT [15], KT-LVD [19], and TDCI [22] methods are selected as comparison methods. The number of pulses, range cells, and searching fold factors are denoted by M, N, and N_n, respectively. In TDCI method, fold factor search is performed using a blind speed of $v_m = \lambda f_p/4$, and the number

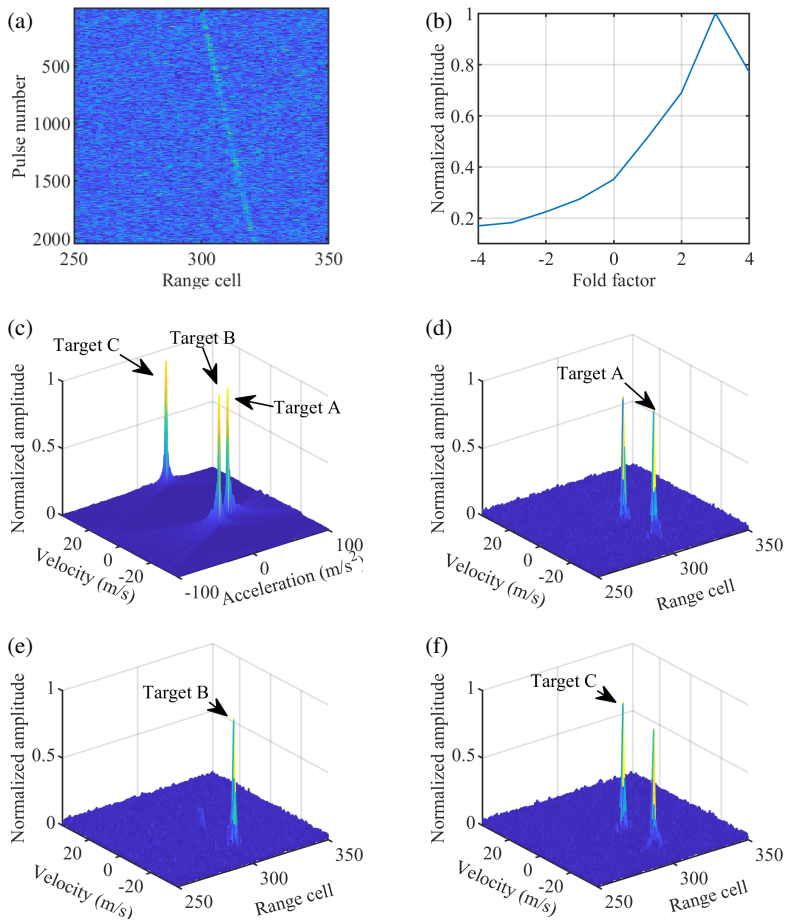

FIGURE 4. Processing results for multiple targets. (a) Result after PC. (b) Fold factor search result. (c) Acceleration estimation result. (d) Coherent integration result of target A. (e) Coherent integration result of target B. (f) Coherent integration result of target C.

of fold factor searches is given by $2N_n$. To ensure a fair comparison, we use the same parameter range and estimation accuracy for all four methods. In this case, the numbers of search velocities and accelerations for GRFT should be set to MN_n and M, respectively [22].

According to [5, 19, 22], the computational complexity of GRFT is $\mathrm{O}(M^3NN_n)$. For KT-LVD method, the computational complexity of KT based on chirp Z-transform (CZT) is $\mathrm{O}(4MN\log_2 M)$. Next, the computational complexity of the fold factor search is $\mathrm{O}(N_nMN\log_2 N)$. Finally, the computational complexity of the CZT-based LVD is $\mathrm{O}(M^2 + 4M^2\log_2 M)$.

Table 4 presents the computational complexity of each major step in TDCI and KT-ITDCI. Compared with GRFT, both TDCI and KT-ITDCI demonstrate lower computational complexity. Moreover, KT-ITDCI further reduces computational complexity based on TDCI. The main computational complexity of TDCI lies in NUFFT, SFT, and IFFT operations, with a total complexity of $\mathrm{O}[(8N_n+2)M^2N\log_2 M]$. In contrast, the main computational complexity of KT-ITDCI is concentrated in the NUFFT, FFT, and IFFT operations, with a total complexity of $\mathrm{O}[(2N_n+2)M^2N\log_2 M]$. Therefore, the computational complexity of KT-ITDCI is approximately one-fourth of that of TDCI. The KT-LVD method exhibits the lowest computational complexity, as it avoids multi-dimensional parameter search and only requires processing a 2-D AF.

TABLE 4. Computational complexity of TDCI and KT-ITDCI.

Step \ Methods	TDCI	KT-ITDCI
KT	–	$\mathrm{O}(4MN\log_2 M)$
AF	$\mathrm{O}(M^2N)$	$\mathrm{O}(M^2N)$
NUFFT	$\mathrm{O}(2M^2N\log_2 M)$	$\mathrm{O}(2M^2N\log_2 M)$
DP	$\mathrm{O}(M^2N)$	$\mathrm{O}(M^2N)$
UC	$\mathrm{O}(2N_nM^2N)$	$\mathrm{O}(N_nM^2N)$
SFT	$\mathrm{O}(6N_nM^2N\log_2 M)$	–
FFT	–	$\mathrm{O}(N_nM^2N\log_2 M)$
IFFT	$\mathrm{O}(2N_nM^2N\log_2 N)$	$\mathrm{O}(N_nM^2N\log_2 N)$

The following simulations are conducted to verify the differences in computational complexity among the methods. As shown in Table 5, for example, when M is equal to 512, it can be observed that KT-ITDCI requires 77.9 s, whereas TDCI takes 273.5 s, and GRFT takes 39502.3 s. Notably, KT-LVD requires only 0.5 s, achieving the lowest execution time among all methods. KT-ITDCI's execution time reduction in MAT-

Methods \ Pulse number	128	256	512
KT-LVD (s)	0.1	0.2	0.5
TDCI (s)	15.6	63.9	273.5
GRFT (s)	751.2	5821.8	39502.3
KT-ITDCI (s)	4.2	17.7	77.9

*Main configuration of the computer: CPU: AMD Ryzen 7 7840H 3.8 GHz; RAM: 32 GB; Operating System: Windows 11; Software: Matlab 2023a.

TABLE 5. Execution times of each method.

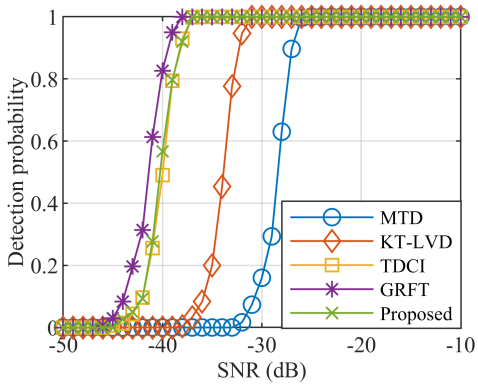

FIGURE 5. Detection probability of MTD, GRFT, TDCI and KT-ITDCI.

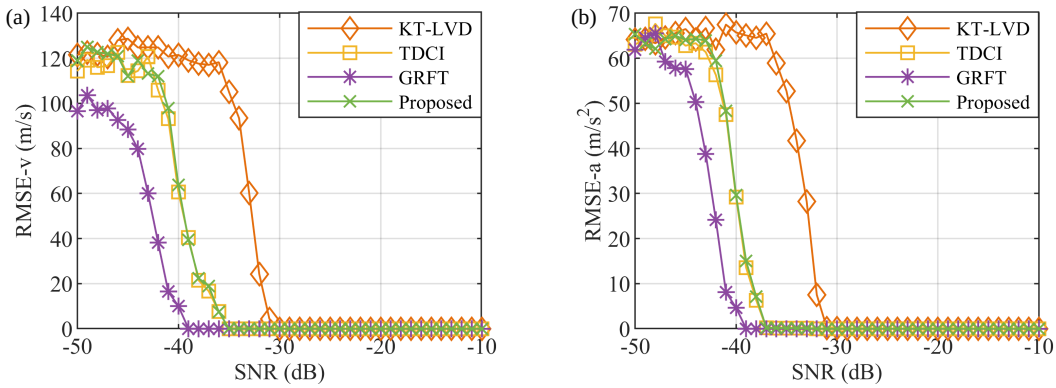

FIGURE 6. MSE curves. (a) RMSEs of velocity estimates. (b) RMSEs of acceleration estimates.

LAB differs from Table 4's theoretical predictions, mainly because MATLAB's FFT and matrix multiplication are highly optimized.

4.4. Anti-Noise Performance

To evaluate detection performance under noisy conditions, a CFAR detector is applied to each method. The simulation parameters are consistent with those listed in Tables 1 and 2.

To further demonstrate the effectiveness of the proposed method, it is also compared against the moving target detection (MTD) method. The SNR ranges from -50 dB to -10 dB, with 300 Monte Carlo trials conducted for each SNR level. Fig. 5 shows the detection probability of each method as a function of SNR at a false alarm probability of 10^{-6}. As shown in Fig. 5, the proposed method achieves comparable anti-noise performance to that of TDCI. However, it exhibits a performance degradation of approximately 1 dB compared with GRFT, while achieving a 6 dB improvement over KT-LVD and an 11 dB improvement over MTD.

4.5. Parameter Estimation Accuracy

In this subsection, the parameter estimation accuracy is evaluated using root mean square error (RMSE) as the evaluation metric. The corresponding RMSE results are presented in Fig. 6.

As shown in Fig. 6, GRFT method achieves the highest estimation accuracy due to its multi-dimensional parameter search process. TDCI and KT-ITDCI exhibit comparable estimation accuracy. However, the proposed method significantly reduces computational complexity. In contrast, KT-LVD demonstrates the lowest estimation accuracy among all the evaluated methods.

The default maximum acceleration estimation value in the simulations is set to 100 m/s^2, corresponding to a scaling factor of $h = 2.67$ and an estimation accuracy of 0.20 m/s^2. The impact of the scaling factor on performance was evaluated by conducting additional simulations with maximum acceleration values of 50 m/s^2 and 200 m/s^2. Detection probability and acceleration estimation performance were compared accordingly.

As shown in Fig. 7, under low SNR conditions, the RMSE of acceleration estimation increases with the expansion of the estimation range. However, the minimum detectable SNR corresponding to a detection probability of 1 remains -37 dB across different scaling factors, indicating that the impact of the scaling factor on overall detection performance is limited.

4.6. Coherent Integration for Real Data

The proposed method is further validated using real radar data for unmanned aerial vehicle (UAV) targets detecting in the presence of ground clutter, as described in [23]. The target motion parameters are as follows: a range of 1.28 km, a velocity of -40.42 m/s, and an acceleration of -0.45 m/s^2. The radar sys-

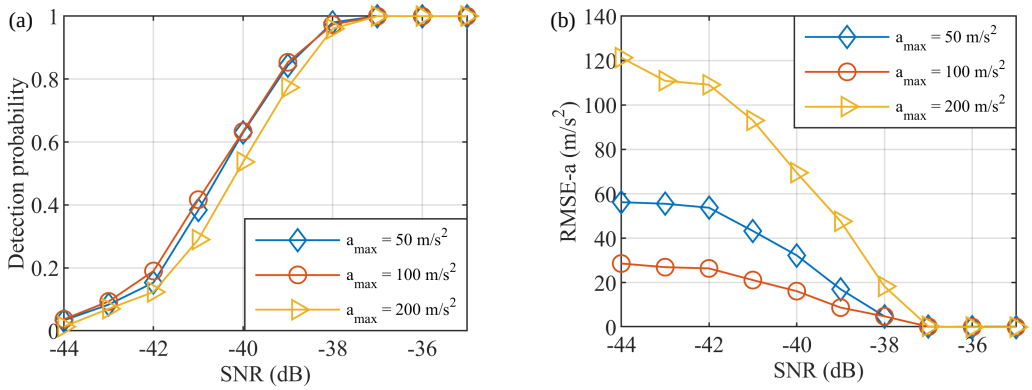

FIGURE 7. Detection probability and acceleration estimation performance under different acceleration estimation ranges. (a) Detection probability. (b) RMSEs of acceleration estimates.

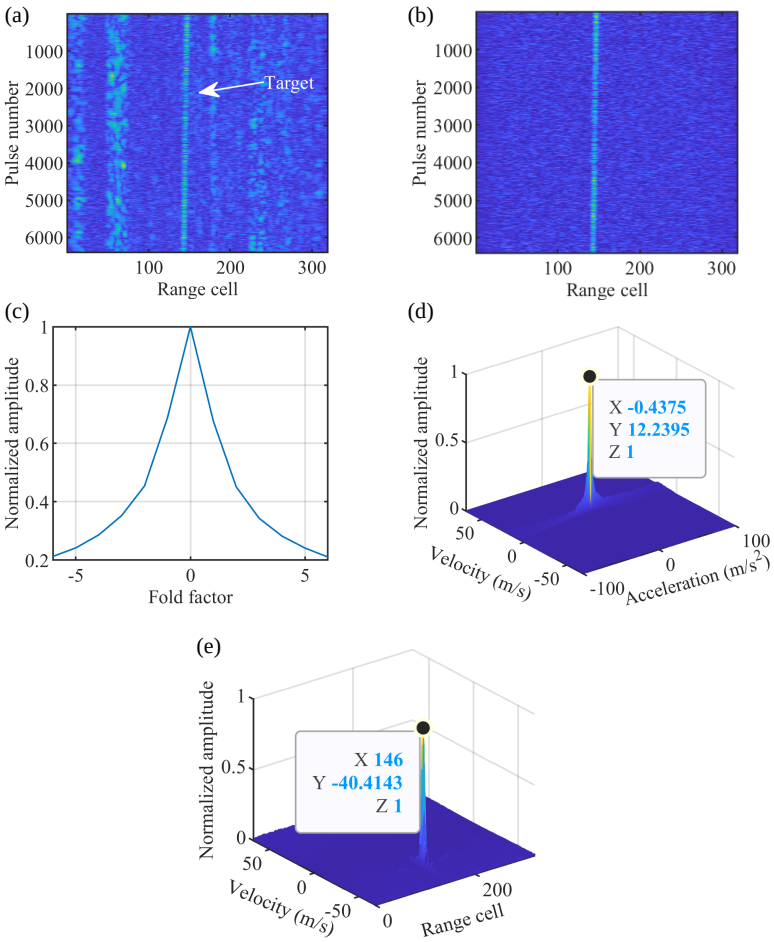

FIGURE 8. Processing results of the real data. (a) Result after PC and MTI. (b) Fold factor search result. (c) Acceleration estimation result. (d) Coherent integration result.

tem parameters are as follows: a carrier frequency of 35 GHz, a sampling frequency of 80 MHz, and a PRF of 32 kHz.

After PC, the result shown in Fig. 8(a) reveals significant ground clutter in the echo signal. Fig. 8(b) presents the result after moving target indication (MTI), indicating that the ground clutter has been effectively suppressed. The processing results of the proposed method are presented in Figs. 8(c)–(e), where the estimated parameters are close to the true values, confirming that KT-ITDCI method effectively processes real radar data.

5. CONCLUSION

To address the challenges of RM and DFM in long-term coherent integration for maneuvering targets, this paper introduces a novel method based on KT-ITDCI. KT-ITDCI not only eliminates the RM induced by unambiguous velocity through KT, but also compensates for residual RM and DFM in the KT-processed echoes via ITDCI, ultimately achieving coherent integration. Experimental results demonstrate that the proposed

method achieves anti-noise performance comparable to that of TDCI, while significantly reducing the computational complexity relative to TDCI. Moreover, compared with TDCI, KT-ITDCI offers more flexible parameter estimation capabilities. The effectiveness of the proposed method is further validated through real-world radar data processing. Future research may further validate the KT-ITDCI method using more real radar data and comprehensive numerical stability analyses, as well as explore coherent integration techniques for targets exhibiting motion orders higher than acceleration.

REFERENCES

[1] Huang, P., G. Liao, Z. Yang, X.-G. Xia, J.-T. Ma, and J. Ma, "Long-time coherent integration for weak maneuvering target detection and high-order motion parameter estimation based on keystone transform," *IEEE Transactions on Signal Processing*, Vol. 64, No. 15, 4013–4026, Aug. 2016.

[2] Sun, Z., X. Li, W. Yi, G. Cui, and L. Kong, "Detection of weak maneuvering target based on keystone transform and matched filtering process," *Signal Processing*, Vol. 140, 127–138, Nov. 2017.

[3] Zheng, J., J. Zhang, S. Xu, H. Liu, and Q. H. Liu, "Radar detection and motion parameters estimation of maneuvering target based on the extended keystone transform (July 2018)," *IEEE Access*, Vol. 6, 76 060–76 074, 2018.

[4] Lin, L., G. Sun, Z. Cheng, and Z. He, "Long-time coherent integration for maneuvering target detection based on ITRT-MRFT," *IEEE Sensors Journal*, Vol. 20, No. 7, 3718–3731, Apr. 2020.

[5] Jin, K., G. Li, T. Lai, T. Jin, and Y. Zhao, "A novel long-time coherent integration algorithm for doppler-ambiguous radar maneuvering target detection," *IEEE Sensors Journal*, Vol. 20, No. 16, 9394–9407, Aug. 2020.

[6] Zhang, J., T. Su, J. Zheng, and X. He, "Novel fast coherent detection algorithm for radar maneuvering target with jerk motion," *IEEE Journal of Selected Topics in Applied Earth Observations and Remote Sensing*, Vol. 10, No. 5, 1792–1803, May 2017.

[7] Huang, X., L. Zhang, S. Li, and Y. Zhao, "Radar high speed small target detection based on keystone transform and linear canonical transform," *Digital Signal Processing*, Vol. 82, 203–215, 2018.

[8] Xu, Z. and G. Zhou, "Long-time coherent integration for radar detection of manoeuvring targets based on accurate range evolution model," *IET Radar, Sonar & Navigation*, Vol. 17, No. 10, 1558–1580, 2023.

[9] Li, S., Y. Wang, B. Wang, G. Battistelli, L. Chisci, and G. Cui, "Efficient dual-scale generalized radon-fourier transform detector family for long time coherent integration," *IEEE Transactions on Signal Processing*, Vol. 72, 4237–4252, 2024.

[10] Xu, W., Y. Wang, J. Huang, H. Wang, and J. Cao, "SAF-SFT-SRAF-based signal coherent integration method for high-speed target detecting in airborne radar," *Progress In Electromagnetics Research C*, Vol. 154, 183–190, 2025.

[11] Zhang, S.-S., T. Zeng, T. Long, and H.-P. Yuan, "Dim target detection based on keystone transform," in *IEEE International Radar Conference*, 889–894, Arlington, VA, USA, May 2005.

[12] Xu, J., J. Yu, Y.-N. Peng, and X.-G. Xia, "Radon-Fourier transform for radar target detection, I: Generalized Doppler filter bank," *IEEE Transactions on Aerospace and Electronic Systems*, Vol. 47, No. 2, 1186–1202, Apr. 2011.

[13] Li, X., G. Cui, L. Kong, and W. Yi, "Fast non-searching method for maneuvering target detection and motion parameters estimation," *IEEE Transactions on Signal Processing*, Vol. 64, No. 9, 2232–2244, May 2016.

[14] Li, X., G. Cui, W. Yi, and L. Kong, "Sequence-reversing transform-based coherent integration for high-speed target detection," *IEEE Transactions on Aerospace and Electronic Systems*, Vol. 53, No. 3, 1573–1580, Jun. 2017.

[15] Xu, J., X.-G. Xia, S.-B. Peng, J. Yu, Y.-N. Peng, and L.-C. Qian, "Radar maneuvering target motion estimation based on generalized Radon-Fourier transform," *IEEE Transactions on Signal Processing*, Vol. 60, No. 12, 6190–6201, Dec. 2012.

[16] Chen, X., J. Guan, N. Liu, and Y. He, "Maneuvering target detection via Radon-fractional Fourier transform-based long-time coherent integration," *IEEE Transactions on Signal Processing*, Vol. 62, No. 4, 939–953, 2014.

[17] Li, X., G. Cui, W. Yi, and L. Kong, "Coherent integration for maneuvering target detection based on Radon-Lv's distribution," *IEEE Signal Processing Letters*, Vol. 22, No. 9, 1467–1471, 2015.

[18] Rao, X., H. Tao, J. Su, J. Xie, and X. Zhang, "Detection of constant radial acceleration weak target via IAR-FRFT," *IEEE Transactions on Aerospace and Electronic Systems*, Vol. 51, No. 4, 3242–3253, 2015.

[19] Li, X., G. Cui, W. Yi, and L. Kong, "Manoeuvring target detection based on keystone transform and Lv's distribution," *IET Radar, Sonar & Navigation*, Vol. 10, No. 7, 1234–1242, 2016.

[20] Li, X., Z. Sun, W. Yi, G. Cui, L. Kong, and X. Yang, "Computationally efficient coherent detection and parameter estimation algorithm for maneuvering target," *Signal Processing*, Vol. 155, 130–142, 2019.

[21] Zheng, J., H. Liu, J. Liu, X. Du, and Q. H. Liu, "Radar high-speed maneuvering target detection based on three-dimensional scaled transform," *IEEE Journal of Selected Topics in Applied Earth Observations and Remote Sensing*, Vol. 11, No. 8, 2821–2833, Aug. 2018.

[22] Zhao, L., H. Tao, and W. Chen, "Maneuvering target detection based on three-dimensional coherent integration," *IEEE Access*, Vol. 8, 188 321–188 334, 2020.

[23] Song, Z., B. Hui, H. Fan, J. Zhou, Y. Zhu, K. Da, X. Zhang, H. Su, W. Jin, Y. Zhang, C. Yang, Z. Lin, and R. Fan, "A dataset for dim target detection and tracking of aircraft in radar echo sequences," Science Data Bank, 2019. [Online]. Available: https://doi.org/10.57760/sciencedb.908.